Adetunji, A.Q., et al., 2023, Crustal conductivity footprint of the orogenic gold district in the Red Lake greenstone belt, western Superior craton, Canada: Geology, https://doi.org/10.1130/G50660.1

Supplemental Material for

Crustal conductivity footprint of the orogenic gold district in the Red Lake Greenstone Belt, western Superior Craton, Canada

Ademola Q. Adetunji[1*], Gaetan Launay[1], Ian J. Ferguson[2], Jack M. Simmons[1], Chong Ma[1], John Ayer[1] and Bruno LaFrance[1]

[1] Mineral Exploration Research Centre, Laurentian University, Sudbury, Ontario, Canada.

[2] Department of Earth Sciences, University of Manitoba, Winnipeg, Manitoba, Canada.

[*] Corresponding author at: Metal Earth, MERC, Laurentian University, 935 Ramsey Lake Road, Sudbury, ON, P3E 2C6, Canada.

Email address: aadetunji@laurentian.ca

1. Magnetotelluric survey and data

As part of the Metal Earth project (Hill et al., 2021 and others), five-component, broadband MT (BBMT) data were collected at 45 sites in fall 2020 by Quantec Geoscience Limited, along the Red Lake transect. The profile is approximately coincident with the central part of the Lithoprobe seismic profile WS2B (Calvert et al., 2004) through the Red Lake gold district. The MT profile was extended to the northern end of the seismic line with five BBMT sites from the previous Lithoprobe Western Superior Transect (Ferguson et al., 2005). The five sites are red-063s, red-064s, red-065a, red-066a, and red-200c and have data with the same period range as the newly acquired dataset (Fig. 1). There is no available MT data to cover the southern extension of the WS2B.

Data were recorded for 48 hours in the period range of ~0.0025 s to 2,500 s at stations spaced at ~2.5 km along the 120 km long profile. Sites occupied on both sides of the main profile were used to provide some 3D control (Fig. 1). Instruments consisted of RT160Q Quantec data logger, Phoenix Geophysics' PE5 non-polarizing electrodes, and Phoenix MTC50 (3000's) and MTC80 magnetic field sensors. Data were processed with the Quantec proprietary QuickLay software coupled with Egbert MT processing code (Egbert, 1997). MT data quality from the Metal Earth survey generally varies from very good to bad at some sites due to excessive cultural noise; data were edited to remove spurious data points and outliers. The vertical magnetic field (tipper) data were edited to exclude power line effects, responses with large error estimates, and responses with magnitudes greater than |0.5|. Some of the tipper data were noisy because of noise from the abundant infrastructure in the region.

2. Dimensionality and inversion

The phase tensor (PT) skew (β), provides a measure of three-dimensionality of the MT response. Absolute skew values (|β|) greater than 3 are indicative of 3D structure (Booker, 2014) and Caldwell et al. (2004) indicate that β is zero in one- and two-dimensional environments. Figure S2 shows the PT plot for the area with almost all the sites showing $|\beta| > 3$ for all periods which is indicative of large-scale 3D structures and justifies 3D inversion.

The three-dimensional signatures exhibited by the data at all stations (as shown in Fig. S1) justifies a 3D inversion approach. Although, some stations were added to increase 3D control, the profile form of the station layout is not optimal for 3D inversion. However, Siripunvaraporn (2012) describes advantages of using 3D inversion for profile data. 3D resistivity models were created using the ModEM algorithm (Egbert and Kelbert, 2012; Kelbert et al., 2014). The initial input data consisted of all the six components of the MT transfer functions for 50 sites from 0.0025s to 1,000 s. After experimenting with different combinations of error floors, the inversions used error floors of 5% imposed on all four impedance components and 0.03 on tipper. The model domain consists of 126 x 96 x 50 cells in the x, y, z-directions respectively. The inner grid of the horizontal cells were 1.5 x 1.5 km in dimension and increased outwardly by a factor of 1.3. The first layer had a thickness of 40 m which increased vertically by a factor of 1.2. A 1,000 Ω.m homogenous half space was chosen as the final starting model as it produced the smallest global misfits for all data components. The smoothing (covariance) parameter, which controls the model smoothness was tested for values ranging from 0.1 – 0.8 and a final smoothing parameter of 0.2 was chosen as it produced the most geologically meaningful model. Three of the stations (RL 18, RL 25, and RL 31) were eventually excluded from the inversion.

The preferred model converged after 118 iterations with a global normalized root-mean-misfit (nRMS) of 1.96 and with nRMS values of 1.69 and 2.8 for the impedance and tipper respectively

(Fig. S2). Figure S3 compares observed and model responses of all components for some representative sites over important conductive feature - C0. The data fit is considered acceptable. The model provides a superior fit to the phase than the apparent resistivity responses (providing an indication of the robustness of the model), but with a slightly poorer fit to the tipper responses. Horizontal and vertical slices of the preferred resistivity model are shown in Figures S4 and S5 with the conductive and resistive features labelled using the same scheme as used for Figure 2.

3. Inversion model hypothesis testing

Model resolution tests were conducted to assess the robustness of the imaged resistivity features in the 3D inversion model, especially the large-scale conductivity anomaly and the interpreted fluid pathways. Forward modelling tests, in which the mid-lower crustal depth was replaced by background resistivity of 1,000 Ω.m were done to evaluate the data components that are sensitive to the large-scale conductivity anomaly. The resultant individual site misfits, when compared with the preferred model, shows values that are significantly higher than that of the original model except in the north part of the profile where the change is marginal (Fig. S6). The results indicate the sensitivity of the data at almost all sites to conductor C0.

A more definitive test of the resolution of the geometry of the deeper conductors was done using an inversion with a horizontal tear (a break in the vertical smoothing) in the model at ~10 km depth. The test involved inserting a thin resistive layer and removing smoothing across this layer from the model roughness calculation. The tear-inversion model, with a total nRMS of 2.05 (Fig. S7), suggests that the depth to the top of conductors C0 and C1 as well as the dip of the top of C1 are features required by the MT data as they are similar to the results in previous inversions. It also shows that C3 has a deeper component that cannot be attributed to downward smearing due to model regularization. In a similar approach, a tear was inserted at the ~36 km depth to investigate the depth of C0. The model (Fig. S8), with nRMS of 2.06, shows that the main part of C0 is in the crust, but this does not exclude possible contribution from the mantle. This test again shows that the geometries of C1- C4 are reasonably well resolved.

In the next series of tests, we examined whether other possible structures, different from the previous ones, could explain the deeper C0. The starting model was constrained to include a resistive mid-lower crust with a fixed resistivity of 100,000 Ω.m while the remaining part of the model was allowed to change. The individual site misfits (Fig. S9) are significantly larger than previous inversion runs, and shows that a C0 conductor located between 20 and 40 km depth is a first order feature that is required to properly fit the MT data.

In summary, the tests indicate that the conductivity associated with C0 must be mainly at middle-lower crustal depths. The resistivity models show that its geometry is constrained by a number (>20) of overlying MT sites. The depth to the top of conductor C1 is resolved at the same location in a number of different models. It is constrained by >5 sites as shown in Figure 2 and Figure S4. The tear inversions show that the conductor extends deeper than 15 km depth and its top is at 10-15 km depth. It is important to note that MT cannot resolve the true thickness of conductors and regularized inversions may cause conductors in MT models to appear thicker than they actually are. Thus, both C0 and C1 may actually be thinner and have a lower resistivity than shown in the figures. The position of C2 is well constrained by the 4 or 5 adjacent MT sites. However, as none of these sites overlie the feature, its geometry is poorly resolved. Although the conductor occurs at depths of 5-10 km in most inversion models, some show it extending deeper, and connecting with C0, but this geometry is not an absolute requirement of the MT data. Also, the first tear model does not show it extending to depth. The true width of the feature may not be

resolved as the horizontal resolution is limited by the MT sites spacing. Conductor C3 is well constrained by the five overlying sites and its depth extent is also shown in the tear inversion models. This feature is consistently imaged as a subvertical structure suggesting its geometry is well resolved. Several inversion models show that C3 is connected to C1. The true width of the feature may again not be resolved. Feature C4 is constrained by two overlying MT sites with weaker constraints coming from some adjacent sites. Its top is at ~5 km depth. The geometry of this feature is reasonably well resolved and some inversions results show that it may also be connected to C0 at depth. Thus, features C0 – C4 are all first order features required by the MT data.

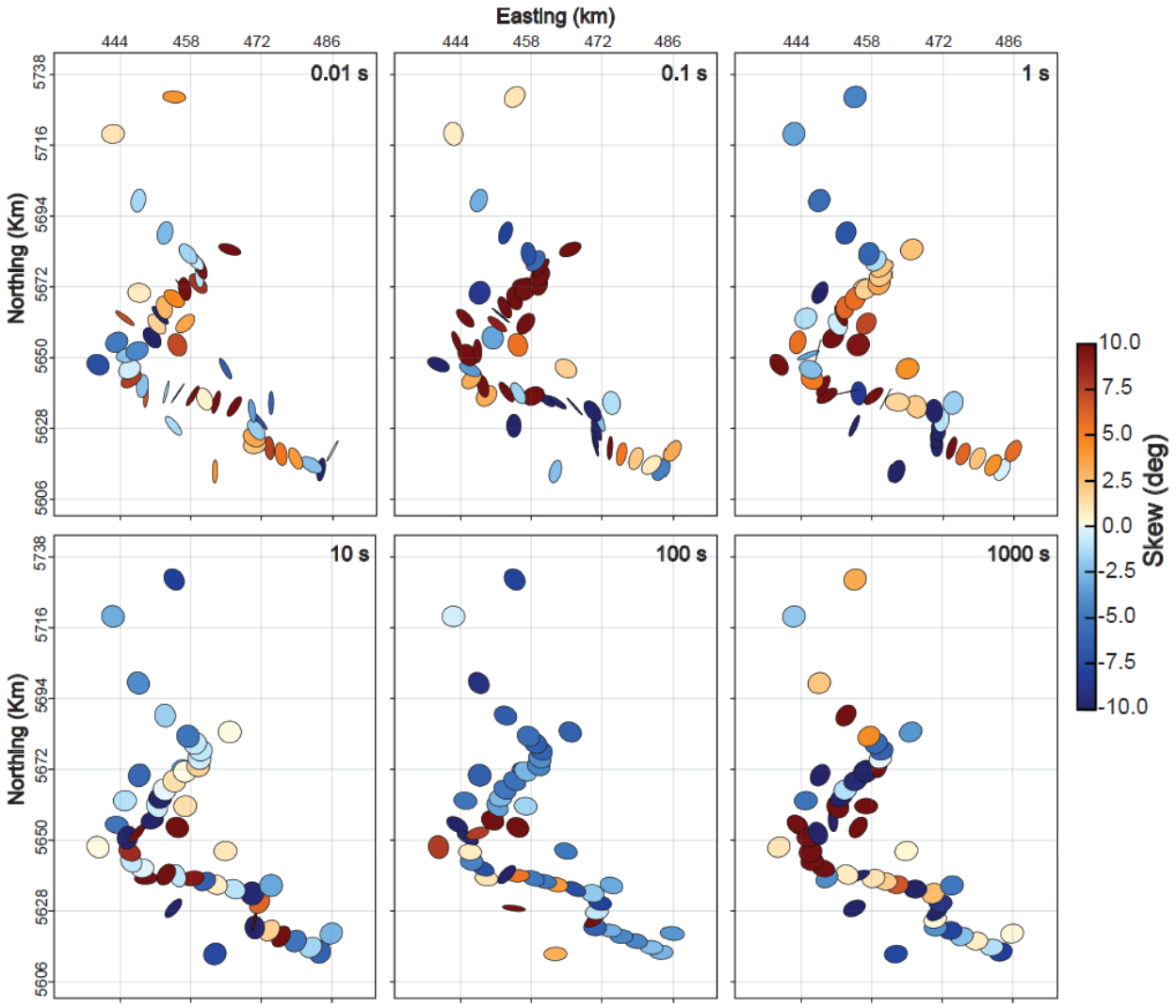

Fig. S1. Phase tensor ellipse for periods between 0.01 and 1000 s. Ellipses are colored using the phase tensor skew β which provides a measure of three-dimensionality. At all periods, almost all sites show $|\beta| > 3$ indicating large scale 3D structures. The ellipticity of the tensors indicate the strength of two-dimensionality, with the long axis of the ellipse showing the direction of Φ_{max} (often the more resistive direction). The induction phase tensors were plotted using MTpy (Kirkby et al., 2019).

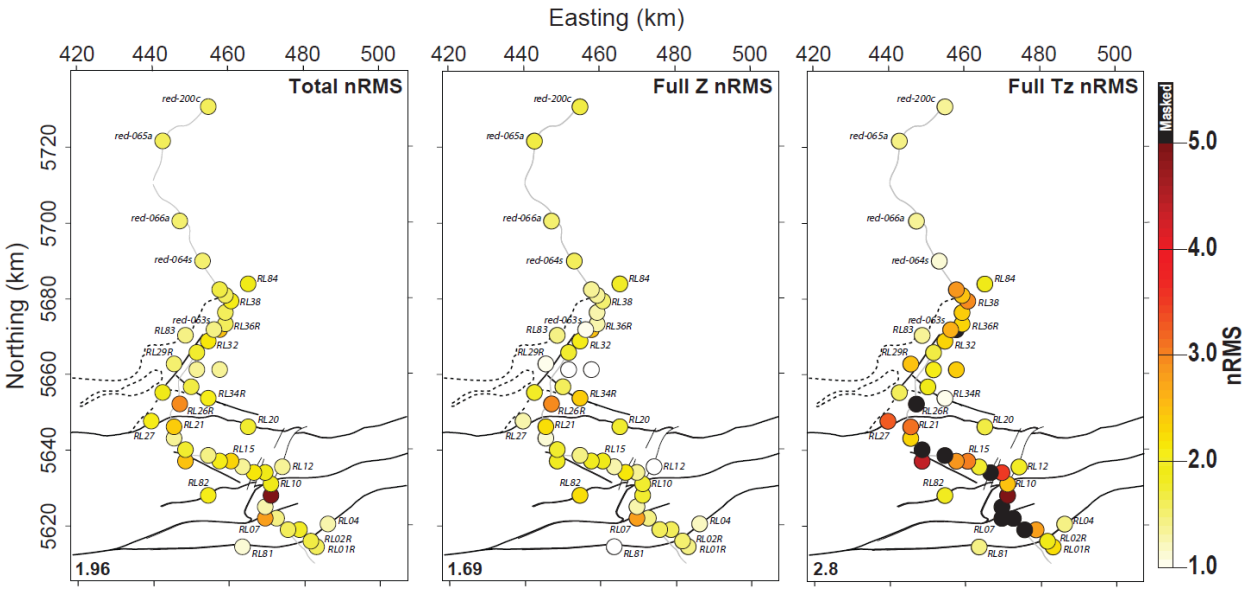

Fig. S2. Data misfits for the preferred 3D MT inversion model. The left panel shows the normalized misfit values (plotted as colored circles at the location of the MT sites) for full impedance tensor and vertical magnetic (tipper) components, the middle panel shows misfits for full impedance tensor components, and the right panel shows values for only vertical magnetic field components. See the main text for the error floors. The black circles on the right panel indicate sites where tipper data were completely excluded from the inversion.

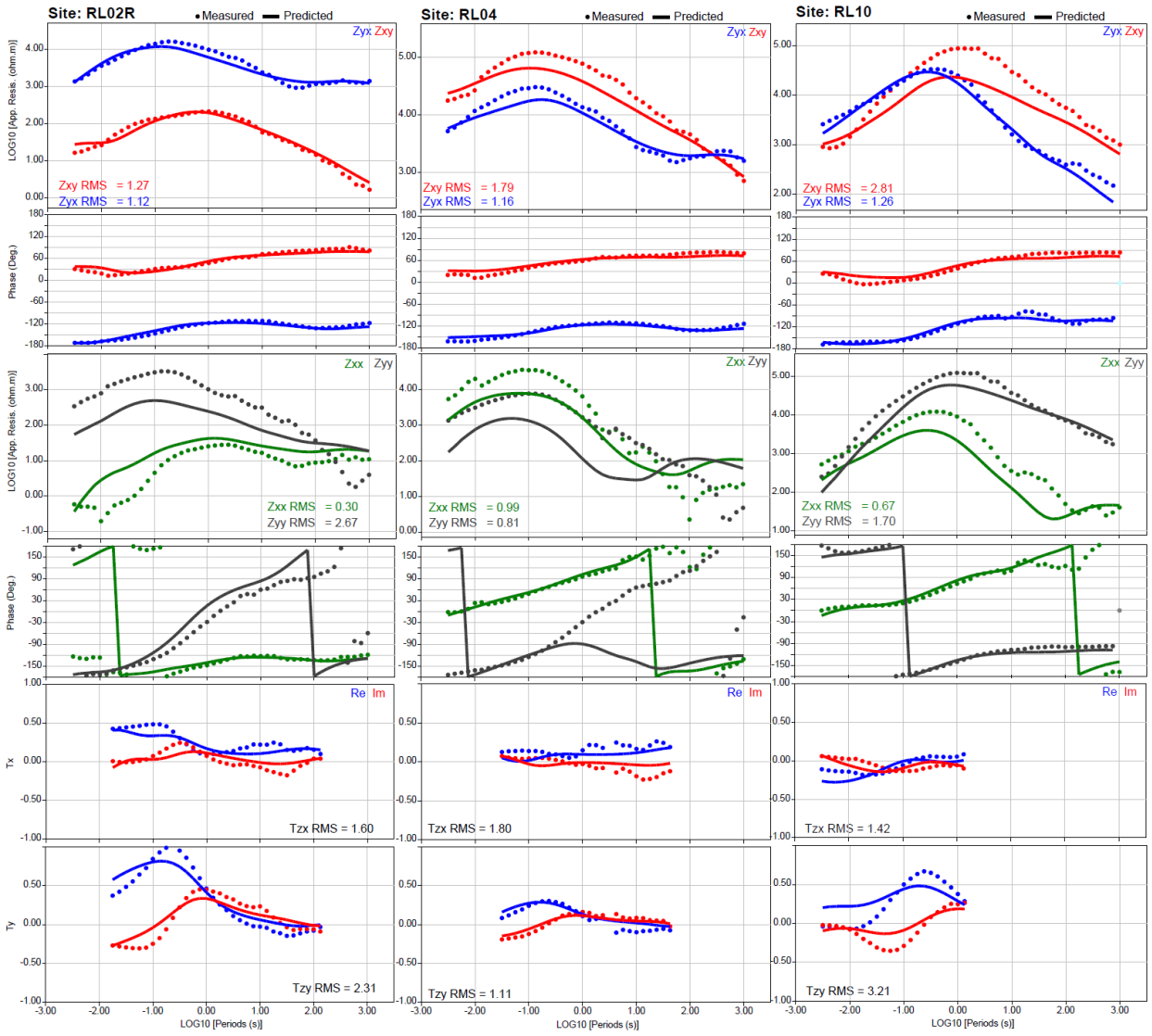
Site: RL02R
Measured
Predicted
Zyx Zxy
LOG10 [App. Resis. (ohm.m)]
Zxy RMS = 1.27
Zyx RMS = 1.12
Phase (Deg.)
Zxx Zyy
Zxx RMS = 0.30
Zyy RMS = 2.67
Re Im
Tx
Tzx RMS = 1.60
Ty
Tzy RMS = 2.31
LOG10 [Periods (s)]
Site: RL04
Measured
Predicted
Zyx Zxy
Zxy RMS = 1.79
Zyx RMS = 1.16
Zxx Zyy
Zxx RMS = 0.99
Zyy RMS = 0.81
Re Im
Tzx RMS = 1.80
Tzy RMS = 1.11
LOG10 [Periods (s)]
Site: RL10
Measured
Predicted
Zyx Zxy
Zxy RMS = 2.81
Zyx RMS = 1.26
Zxx Zyy
Zxx RMS = 0.67
Zyy RMS = 1.70
Re Im
Tzx RMS = 1.42
Tzy RMS = 3.21
LOG10 [Periods (s)]

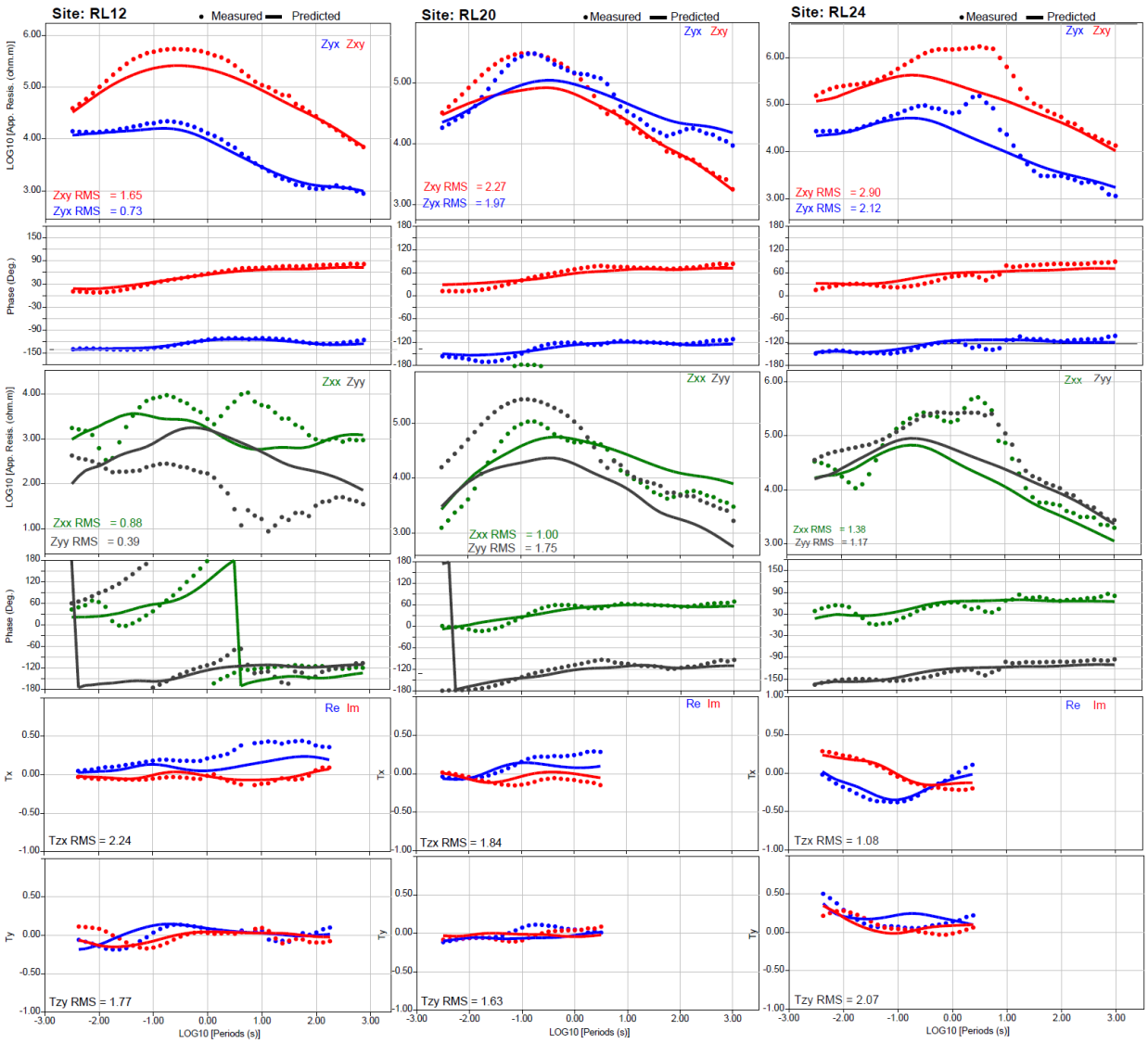

Fig. S3. Observed and predicted sounding curves for the apparent resistivity and phase for diagonal and off-diagonal impedance components as well as vertical magnetic transfer functions for six representative sites located above conductor C0.

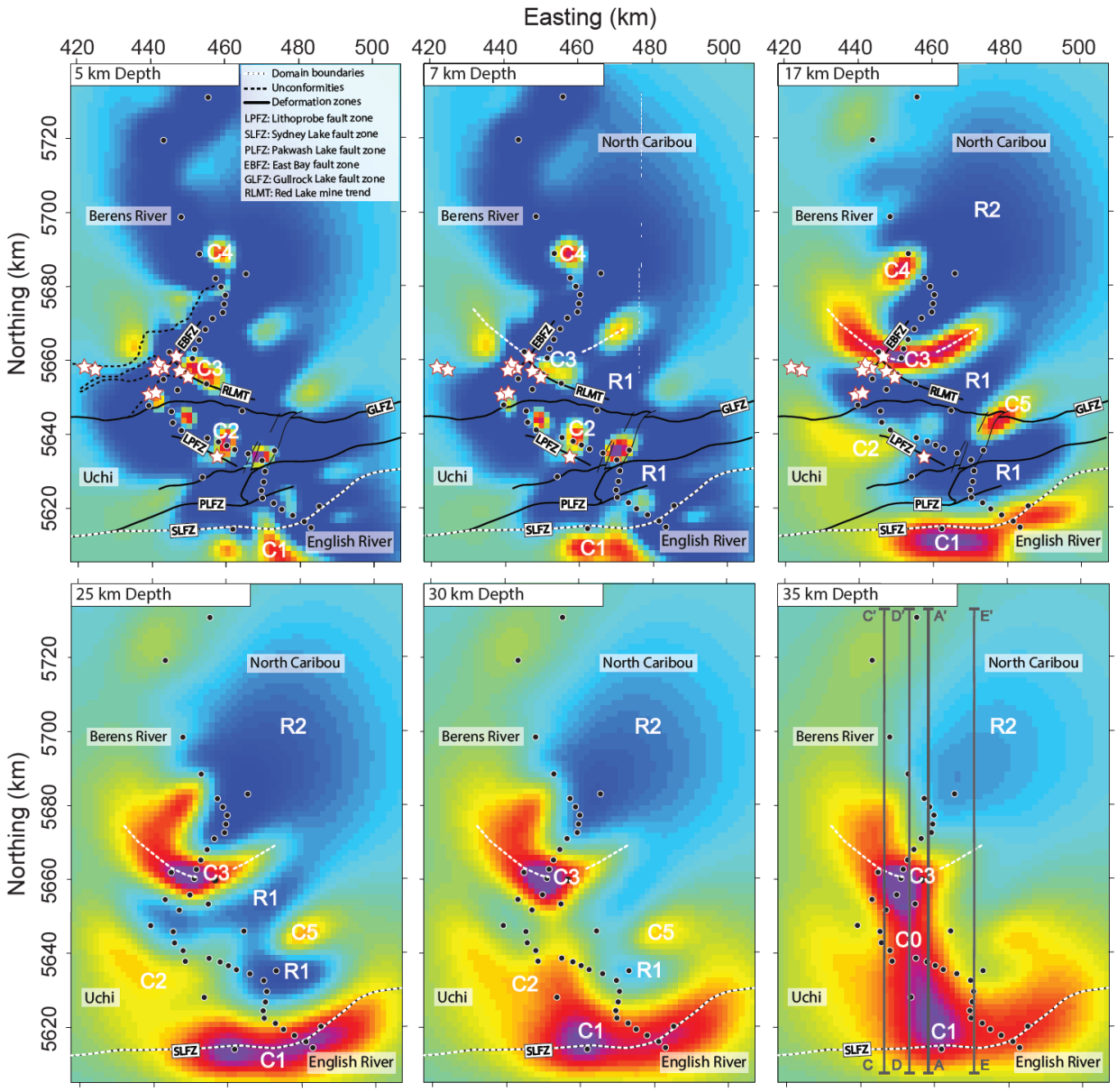

Fig. S4. Selected depth sections of the 3-D resistivity model. Black dots indicate MT station used for the 3-D inversion. Conductive and resistive features labelled using the same scheme as used in Figure 2. Overlain on 35 km panel with black lines are the locations of the vertical sections shown in Figure S5.

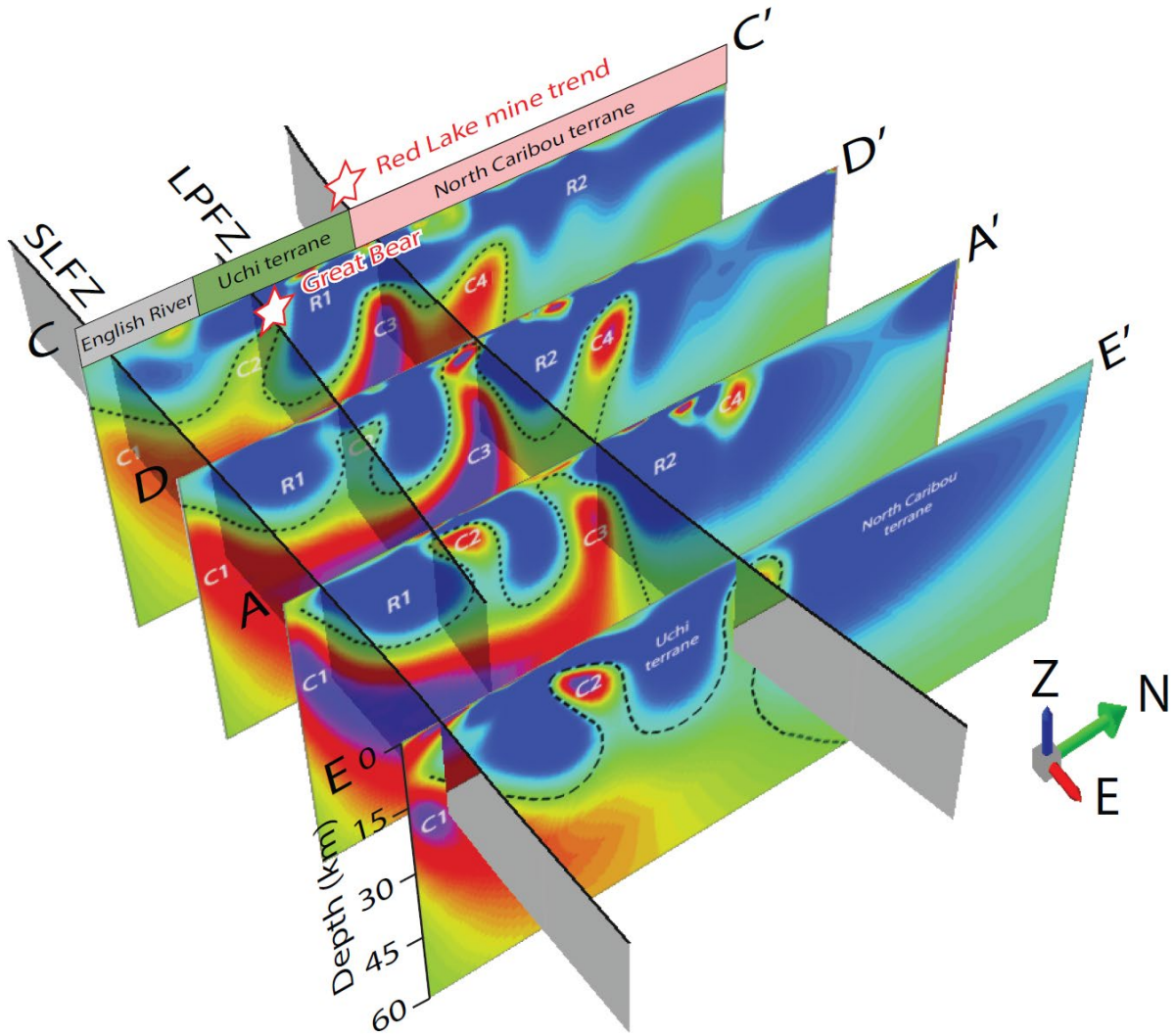

Fig. S5. Vertical slices of the 3D resistivity model showing north-south sections as shown in Figure S4.

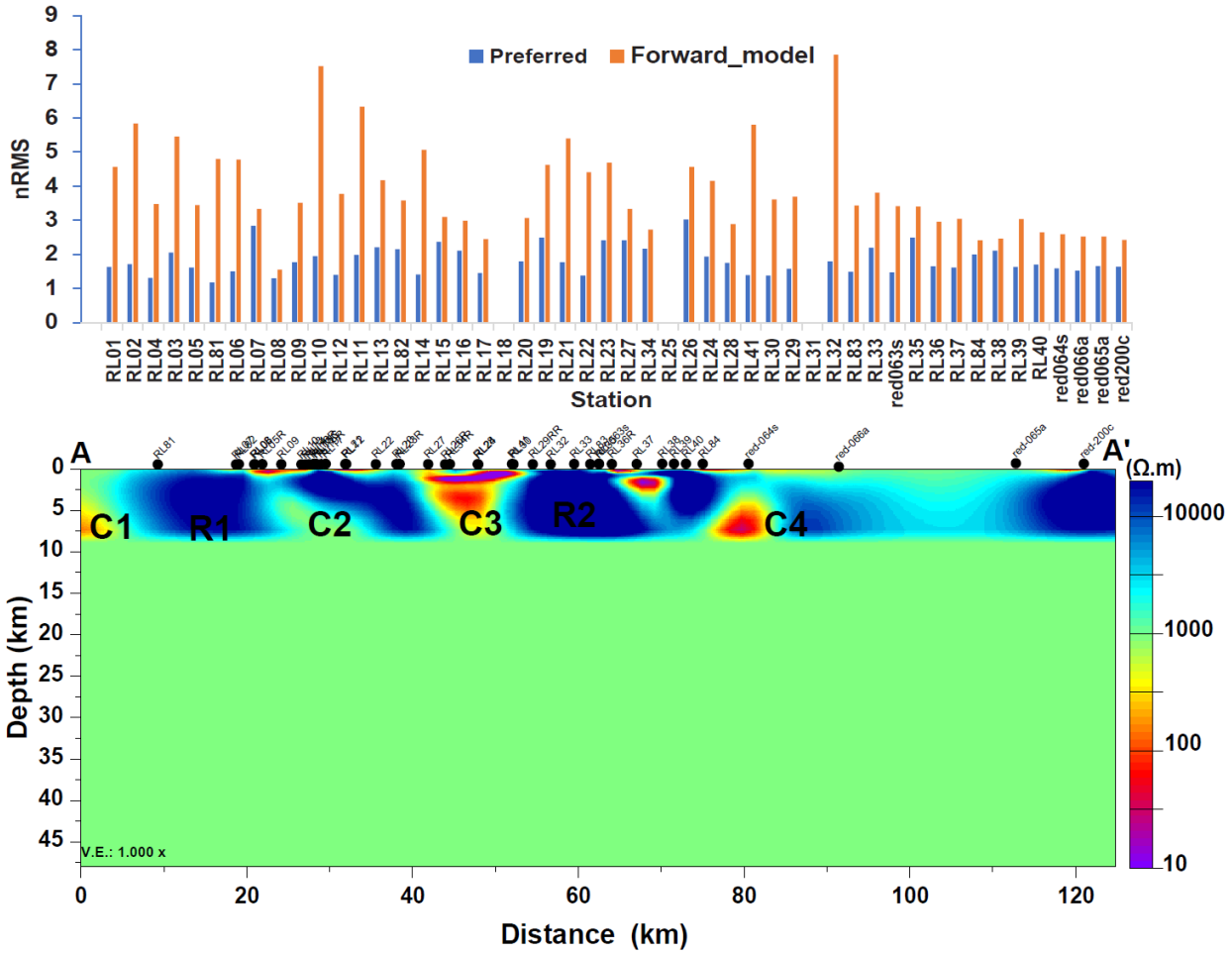

Fig. S6. Comparison of individual nRSM values for the preferred model and the forward modelling response (upper panels) showing the sensitivity of the MT responses to the removal of the large-scale crustal conductor, C0, demonstrating the sensitivity of the responses to this feature. The MT section (lower panel) shows the replacement of the features at depths greater than 9 km with homogenous resistivity of 1,000 Ω.m.

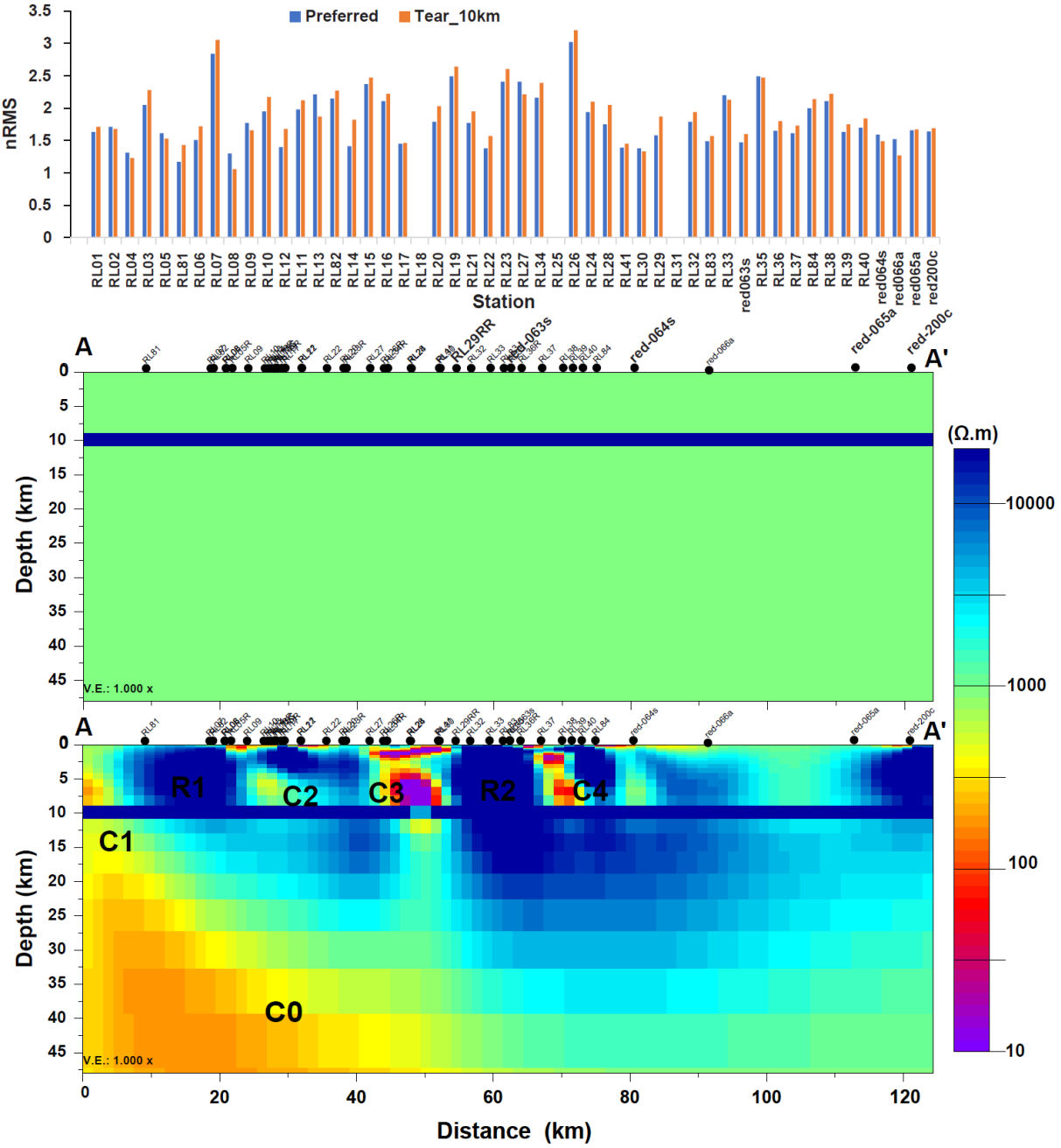

Fig. S7. Cross section of the 3D resistivity model from a tear-inversion. A tear, or break in the vertical smoothing, is created at the thin resistive (100,000 Ω.m) layer located at ~ 10 km depth. Upper panel shows the comparison of individual nRMS values for the preferred model and the constrained model. The middle panel shows north-south vertical section of the constrained model and lower panel shows the final inverse model. The results show that the MT data require the conductor C3 to include a part at >10 km depth and that the deeper parts of this are not caused by downward smearing of the shallow conductors. The similarity of the conductors C1 and C0 in this model with those in the preferred model (Fig. 2) also indicates that the depth to the top of the conductors and the northwards dip of the top of C1 are features required by the MT data set. Total nRMS = 2.05, Z = 1.79 and Tz = 2.87.

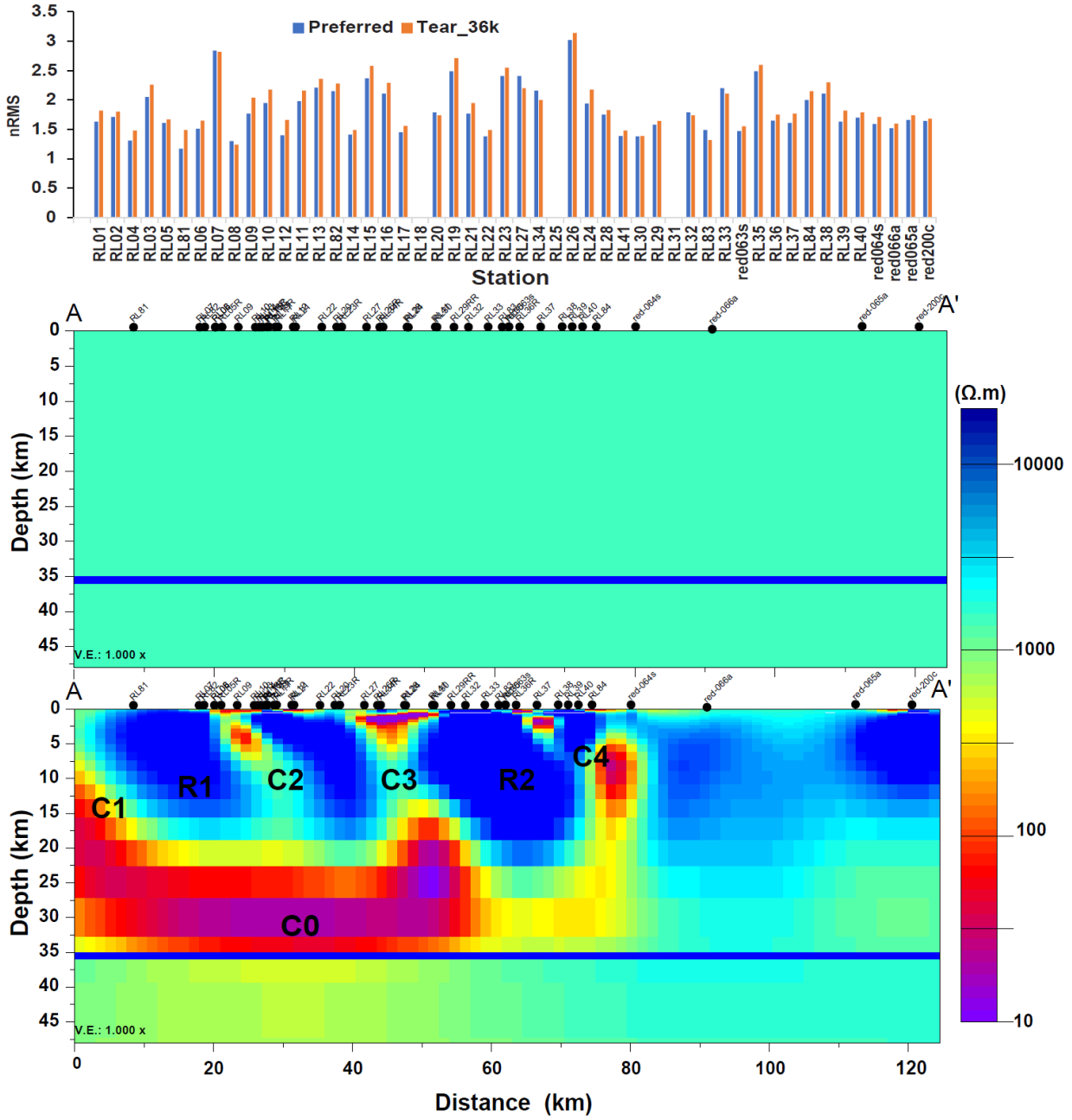

Fig. S8. A tear, or break in the vertical smoothing, is created at the resistive (100,000 Ω.m) layer at ~36 km depth. Total nRMS = 2.06, Z = 1.76 and Tz = 3.00. Upper panel shows the comparison of individual nRMS values for the preferred model and the constrained model. The middle panel shows north-south vertical section of the constrained model and lower panel shows the final inverse model.

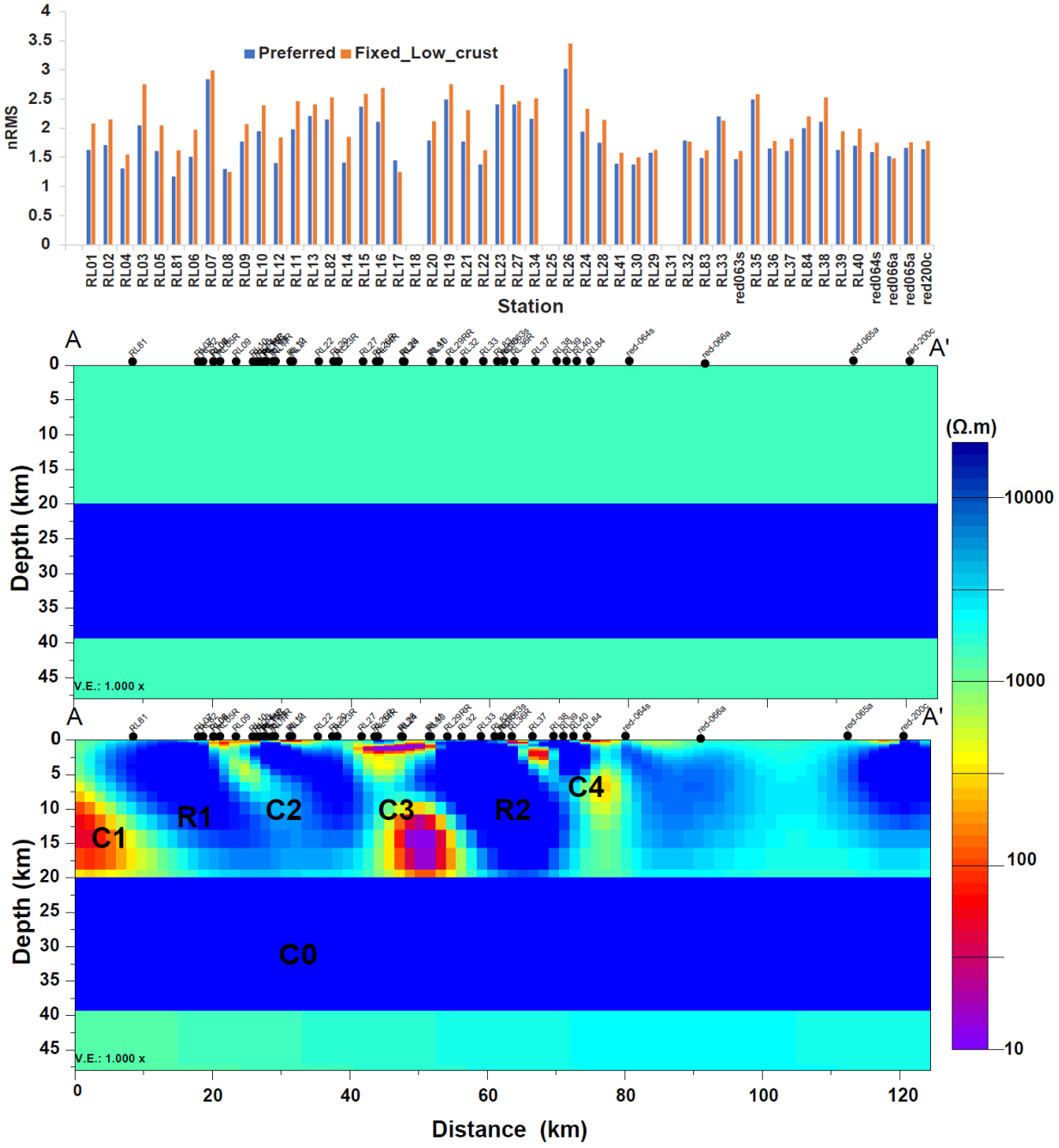

Fig. S9. With lower crustal resistivity between 20 and 40 km depth fixed at 100,000 Ω.m (starting and final models). Total nRMS = 2.22, Z = 1.95 and Tz = 3.10. Upper panel shows the comparison of individual nRSM values for the preferred model and the constrained model. The middle shows north-south vertical section of the constrained model and lower panel shows the inverse model.

References

Booker, J. R., 2014. The magnetotelluric phase tensor: A critical review. Surveys in Geophysics, v. 35, p 7–40.

Caldwell, T. G., Bibby, H. M., Brown, C., 2004. The magnetotelluric phase tensor; Geophysical Journal International, 158, 457–469.

Egbert, G. D., and Kelbert, A., 2012, Computational recipes for electromagnetic inverse problems: Geophysical Journal International, v. 189, p. 251–267, https://doi.org/10.1111/j.1365-246X.2011.05347.x.

Egbert, G.D., 1997. Robust multiple station magnetotelluric data processing. Geophys. J. Int., 130, 475-496.

Ferguson, I.J., Craven, J.A., Kurtz, R.D., Boerner, D.E., Bailey, R.C., Wu, X., Orellana, M.R., Spratt, J., Wennberg, G., Norton, M., 2005, Geoelectric response of Archean lithosphere in the western Superior Province, central Canada. Physics of the Earth and Planetary Interiors, v. 150, p123–143. doi:10.1016/j.pepi.2004.08.025

Hill, G.J., Roots, E.A., Frieman, B.M., Haugaard, R., Craven, J.A., Smith, R.S., Snyder, D. B., Zhou, X., Sherlock, R., 2021, On Archean craton growth and stabilisation: Insights from lithospheric resistivity structure of the Superior Province. Earth and Planetary Science Letters. 562, 116853. https://doi.org/10.1016/j.epsl.2021.116853.

Kelbert, A., Meqbel, N., Egbert, G. D., and Tandon, K., 2014, ModEM: A modular system for inversion of electromagnetic geophysical data: Computers & Geoscience, v. 66, p. 40–53, https://doi.org/10.1016/j.cageo.2014.01.010.

Kirkby, A., Heinson, G., Krieger, L., 2016. Relating permeability and electrical resistivity in fractures using random resistor network models. Journal of Geophysical Research: Solid Earth, 121, 1546-1564.

Siripunvaraporn, Weerachai, 2012. Three-dimensional magnetotelluric inversion: an introductory guide for developers and users. Surveys in Geophysics, v. 33, p 5-27. https:// doi.org/10.1007 /s10712-011-9122-6.